

# Superconductivity with large upper critical field in noncentrosymmetric Cr-bearing high-entropy alloys

Guorui Xiao<sup>1,2,3</sup>, Wuzhang Yang<sup>1,2,4</sup>, Qinqing Zhu<sup>1,2,4</sup>, Shijie Song<sup>3</sup>, Guang-Han Cao<sup>3</sup>, and Zhi Ren<sup>1,2\*</sup>

<sup>1</sup>Department of Physics, School of Science, Westlake University,

18 Shilongshan Road, Hangzhou, 310024, Zhejiang Province, PR China

<sup>2</sup>Institute of Natural Sciences, Westlake Institute for Advanced Study,

18 Shilongshan Road, Hangzhou, 310024, Zhejiang Province, PR China

<sup>3</sup>School of Physics, Zhejiang University, Hangzhou 310058, PR China and

<sup>4</sup>Department of Physics, Fudan University, Shanghai, 200433, PR China

(Dated: February 14, 2023)

A series of new  $\text{Cr}_{5+x}\text{Mo}_{35-x}\text{W}_{12}\text{Re}_{35}\text{Ru}_{13}\text{C}_{20}$  high-entropy alloys (HEAs) have been synthesized and characterized by x-ray diffraction, scanning electron microscopy, electrical resistivity, magnetic susceptibility and specific heat measurements. It is found that the HEAs adopt a noncentrosymmetric cubic  $\beta$ -Mn type structure and exhibit bulk superconductivity for  $0 \leq x \leq 9$ . With increasing  $x$ , the cubic lattice parameter decreases from 6.7940(3) Å to 6.7516(3) Å. Meanwhile, the superconducting transition temperature  $T_c$  is suppressed from 5.49 K to 3.35 K due to the magnetic pair breaking caused by Cr moments. For all these noncentrosymmetric HEAs, the zero-temperature upper critical field  $B_{c2}(0)$  is comparable to Pauli paramagnetic limit  $B_P(0) = 1.86T_c$ . In particular, the  $B_{c2}(0)/B_P(0)$  ratio reaches a maximum of  $\sim 1.03$  at  $x = 6$ , which is among the highest for  $\beta$ -Mn type superconductors.

**Keywords:** high-entropy alloys; noncentrosymmetric structure; superconductivity; magnetic pair breaking; upper critical field.

Recently, the design of alloys based on the high-entropy concept has attracted widespread attention [1–7]. In principle, high-entropy alloys (HEAs) should be single phase solid solutions made up of at least five metallic elements whose atomic concentrations vary between 5% to 35%. These materials are believed to be stabilized by the large configurational entropy and characterized by strong atomic disorder and local lattice distortion. As such, HEAs are commonly referred as metallic glasses on ordered lattices and often exhibit superior mechanical [8, 9], chemical [10–15] and physical [16–20] properties compared with traditional alloys based on one or two elements. Apart from this, the chemical complexity of HEAs allows for a wide tunability in both structure and property, which offers a fertile playground to study their relationship in multicomponent alloy systems.

So far, a number of HEAs have been found to display type-II superconductivity and most of them possess centrosymmetric structural types, such as body-centered-cubic (*bcc*) type [21, 22], CsCl type [23], hexagonal-closed packed (*hcp*) type [24–26], A15 type [27, 28],  $\sigma$  type [29, 30] and face-centered-cubic (*fcc*) type [31]. The  $T_c$  of these HEAs shows a peculiar dependence on the valence electron concentration and is robust against disorder and magnetic impurity. By contrast, the absence of structural inversion symmetry can allow for a mixed spin-singlet and spin-triplet pairing state. However, noncentrosymmetric HEA superconductors have been much less explored and exist only in cubic  $\alpha$ -Mn [32, 33] and  $\beta$ -Mn [34] type structures.

The former examples include  $(\text{ZrNb})_{1-x}(\text{MoReRu})_x$ ,  $(\text{HfTaWIr})_{1-x}\text{Re}_x$  [32],  $(\text{HfTaWPt})_{1-x}\text{Re}_x$  [32],  $\text{Nb}_{25}\text{Mo}_{5+x}\text{Re}_{35}\text{Ru}_{25-x}\text{Rh}_{10}$  [33], while the latter example is limited to  $\text{Ta}_{10}\text{Mo}_5\text{W}_{30}\text{Re}_{35}\text{Ru}_{20}\text{C}_x$  ( $16 \leq x \leq 20$ ) [34], where the interstitial carbon plays a crucial role in stabilizing the structure. Moreover, to our knowledge, no prior study has been conducted to look for noncentrosymmetric HEA superconductors containing magnetic elements.

Here we present the synthesis and characterization of new  $\text{Cr}_{5+x}\text{Mo}_{35-x}\text{W}_{12}\text{Re}_{35}\text{Ru}_{13}\text{C}_{20}$  HEAs. For the first time, a single  $\beta$ -Mn type phase is obtained for  $x$  in the range of 0 to 9. These  $\beta$ -Mn type HEAs become bulk superconductors with  $T_c$  decreasing monotonically from 5.49 K to 3.35 K as the increase of  $x$ , which is attributed to pair breaking due to Cr local moments. Despite the suppression of  $T_c$ , the  $B_{c2}(0)$  for all these HEAs is close to or even slightly exceeds the corresponding  $B_P(0)$ . A comparison is made between the  $B_{c2}(0)/B_P(0)$  ratios of  $\text{Cr}_{5+x}\text{Mo}_{35-x}\text{W}_{12}\text{Re}_{35}\text{Ru}_{13}\text{C}_{20}$  HEAs and ternary  $\beta$ -Mn type superconductors, and its implication is briefly discussed.

Polycrystalline  $\text{Cr}_{5+x}\text{Mo}_{35-x}\text{W}_{12}\text{Re}_{35}\text{Ru}_{13}\text{C}_{20}$  HEAs with  $0 \leq x \leq 12$  were prepared by the arc-melting method. Stoichiometric amounts of high purity Cr (99.95%), Mo (99.9%), W (99.9%), Re (99.99%), Ru (99.9%) and C (99.5%) powders were mixed thoroughly and pressed into pellets in an argon filled glove-box. The pellets were then melted four times in an arc furnace under high-purity argon atmosphere, followed by rapid cooling on a water-chilled copper plate. The crystal structure of resulting samples was characterized by powder X-ray diffraction (XRD) using a Bruker D8 Advance X-ray diffractometer with  $\text{Cu K}\alpha$  radiation. The lattice

\*Electronic address: renzhi@westlake.edu.cn

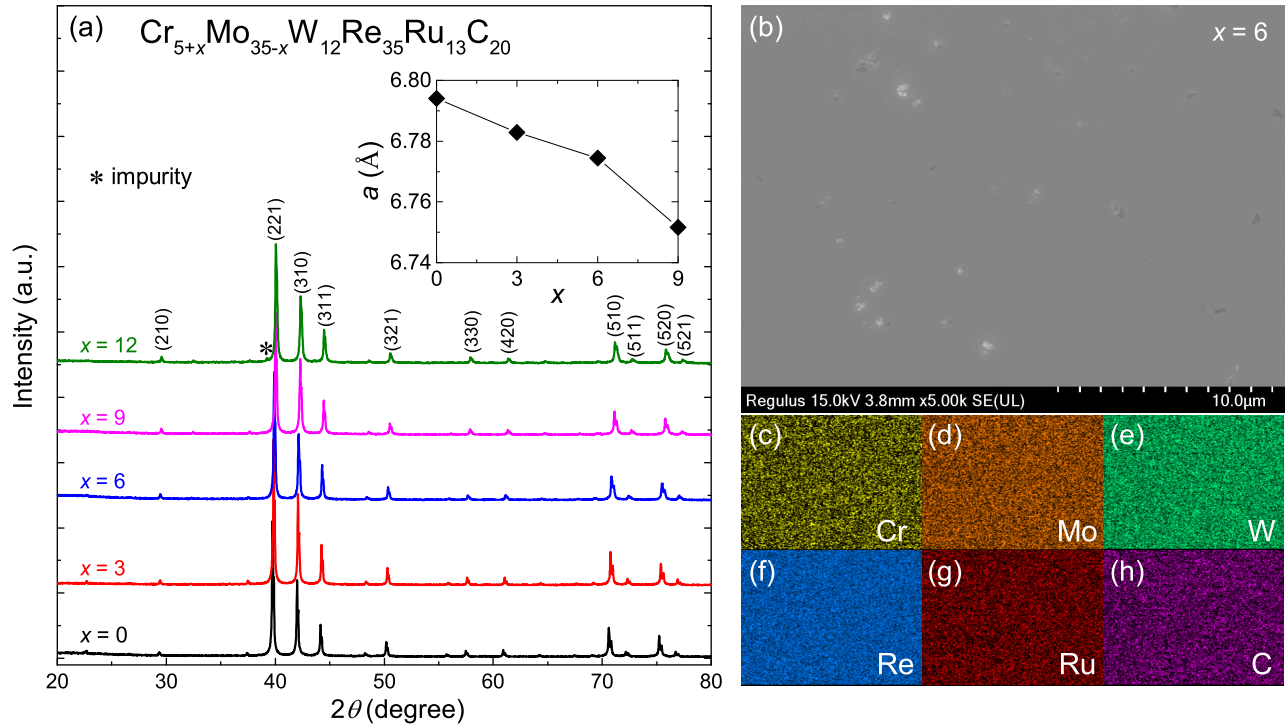


FIG. 1: (a) XRD patterns for the  $\text{Cr}_{5+x}\text{Mo}_{35-x}\text{W}_{12}\text{Re}_{35}\text{Ru}_{13}\text{C}_{20}$  HEAs with increasing  $x$  from 0 to 12. For  $x = 12$ , the major diffraction peaks are indexed and the impurity peak is marked by the asterisk. The inset shows the refined cubic lattice parameter plotted as a function of  $x$ . (b) SEM image for the HEA with  $x = 6$ . (c-h) EDX elemental maps for this HEA.

constant was determined by the Le Bail fitting using the JANA2006 programme [35]. The morphology and chemical composition were investigated in a Hitachi Regulus 8230 field emission scanning electron microscope (SEM) equipped with an energy dispersive X-ray (EDX) spectrometer. Electrical resistivity and specific heat measurements were done in a Quantum Design Physical Property Measurement System (PPMS-9 Dynacool). DC magnetization measurements were carried out in a Quantum Design Magnetic Property Measurement System (MPMS3).

The XRD patterns for the series of  $\text{Cr}_{5+x}\text{Mo}_{35-x}\text{W}_{12}\text{Re}_{35}\text{Ru}_{13}\text{C}_{20}$  HEAs are displayed in Fig. 1(a). For  $x$  varying from 0 to 12, the major diffraction peaks look similar and can be well indexed on the noncentrosymmetric cubic  $\beta$ -Mn type structure with the  $P4_132$  space group. This is confirmed by structural refinement, whose result for  $x = 6$  is shown in Supplementary Fig. S1. Note that all the transition metal atoms are assumed to be distributed randomly in the lattice. Hence the configurational entropies are calculated to be  $1.40R$ ,  $1.45R$ ,  $1.49R$  and  $1.51R$  ( $R = 8.314 \text{ J mol}^{-1} \text{ K}^{-1}$  is the molar gas constant) for  $x = 0, 3, 6$ , and  $9$ , respectively, which are listed in Table I. Nonetheless, a small impurity peak is observed near the (221) peak for  $x = 12$ , and hence the remaining of the paper is focused on the HEAs with  $0 \leq x \leq 9$ . The inset of Fig. 1 (a) shows the refined lattice constants plotted as a function of  $x$ . One can see that the  $a$ -axis decreases from  $6.7940(3) \text{ \AA}$  to  $6.7516(3) \text{ \AA}$  as the increase of  $x$ .

This is as expected since the atomic radius of Cr ( $1.267 \text{ \AA}$ ) is smaller than that of Mo ( $1.386 \text{ \AA}$ ) [36].

Fig. 1(b) shows a typical SEM image for the  $\text{Cr}_{5+x}\text{Mo}_{35-x}\text{W}_{12}\text{Re}_{35}\text{Ru}_{13}\text{C}_{20}$  HEA with  $x = 6$ . Except for a few carbon particles with size below  $1 \mu\text{m}$ , the HEA appears to be dense and homogeneous. This is corroborated by the EDX elemental mapping results displayed in Fig. 1(c)-(h), which reveal a homogeneous distribution of all the constituent elements. In addition, as listed in Table I, the ratios of Cr:Mo:W:Re:Ru are determined to be  $4.7:33.5:12.1:35.8:13.9$ ,  $8.1:31.3:11.4:34.9:14.3$ ,  $11.1:28.5:11.8:34.7:13.9$ , and  $13.3:25.4:11.0:35.7:14.6$  for  $x = 0, 3, 6$ , and  $9$ , respectively. It is obvious that the measured metal stoichiometries are in agreement with the nominal ones within the experimental error. As for carbon, its content cannot be determined accurately by the EDX method due to its light mass.

The low temperature normalized resistivity ( $\rho$ ), magnetic susceptibility ( $\chi$ ) and specific heat ( $C_p$ ) data for the series of  $\text{Cr}_{5+x}\text{Mo}_{35-x}\text{W}_{12}\text{Re}_{35}\text{Ru}_{13}\text{C}_{20}$  HEAs are displayed in Fig. 2(a)-(c). For all  $x$  values, a rapid  $\rho$  drop, a large diamagnetic  $\chi$  and a clear  $C_p$  jump are detected, indicating the occurrence of bulk superconductivity. From the midpoint of  $\rho$  drop,  $T_c$  is determined to be  $5.49 \text{ K}$ ,  $4.73 \text{ K}$ ,  $3.83 \text{ K}$  and  $3.35 \text{ K}$  for  $x = 0, 3, 6$ , and  $9$ , respectively. Below  $T_c$ , there is a obvious divergence between the zero-field cooling (ZFC) and field cooling (FC)  $\chi$  curves, which is characteristic of a type-II superconducting behavior. At  $1.8 \text{ K}$ , the zero-field cool-

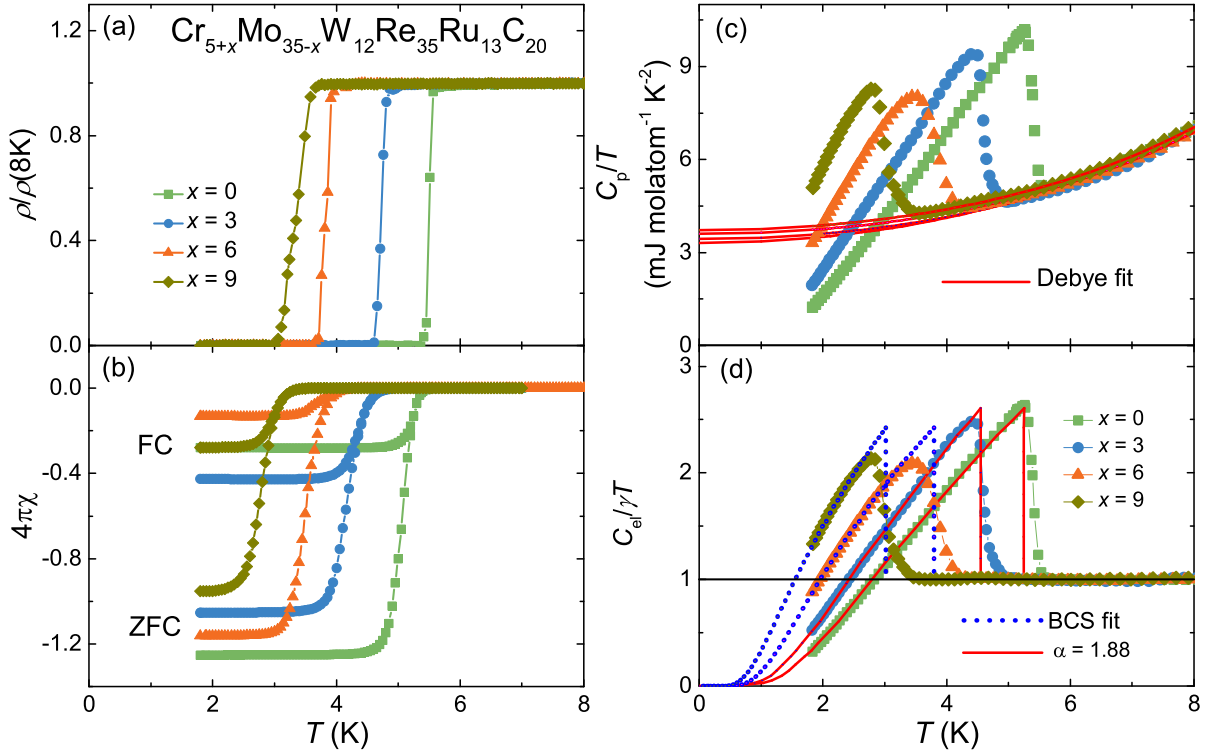


FIG. 2: (a-c) Low temperature normalized resistivity, magnetic susceptibility and specific heat, respectively, for the series of  $\text{Cr}_{5+x}\text{Mo}_{35-x}\text{W}_{12}\text{Re}_{35}\text{Ru}_{13}\text{C}_{20}$  HEAs. In panel (c), the solid lines are Debye fits to the normal-state data. (d) Temperature dependence of normalized electronic specific heat for the HEAs. The dashed and solid lines are fits to the data by the BCS theory and  $\alpha$ -model, respectively.

ing  $\chi$  data correspond to shielding fractions,  $-4\pi\chi$ , in the range of 95-125% without demagnetization correction. In the normal state, the  $C_p$  data can be well fitted by the Debye model,

$$C_p/T = \gamma + \beta T^2 + \delta T^4, \quad (1)$$

where  $\gamma$  and  $\beta$  ( $\delta$ ) are the electronic and phonon specific heat coefficients, respectively. The obtained  $\gamma$  and  $\beta$  values are listed in Table 1. Once  $\beta$  is known, the Debye temperatures  $\Theta_D$  are calculated to be 343 K, 362 K, 368 K and 368 K for  $x = 0, 3, 6$ , and  $9$ , respectively, according to the equation,

$$\Theta_D = (12\pi^4 R/5\beta)^{1/3}. \quad (2)$$

Then the electron-phonon coupling strength  $\lambda_{ep}$  is found to decrease from 0.63 to 0.55 with increasing  $x$  from 0 to 9 based on the inverted McMillan formula [37],

$$\lambda_{ep} = \frac{1.04 + \mu^* \ln(\Theta_D/1.45T_c)}{(1 - 0.62\mu^*) \ln(\Theta_D/1.45T_c) - 1.04}, \quad (3)$$

where  $\mu^* = 0.13$  is the Coulomb repulsion pseudopotential.

Fig. 2(d) shows the normalized electronic specific heat  $C_{el}/\gamma T$  obtained by subtraction of the phonon contribution. For  $x = 6$  and  $9$ , the  $C_{el}/\gamma T$  jump follows nicely

the weak-coupling BCS theory [38]. In comparison, the  $C_{el}/\gamma T$  jumps become larger at  $x \leq 3$ . Hence, to analyze the data, the so called  $\alpha$ -model [39] is employed. This model still assumes a fully isotropic superconducting gap but allows for the variation of coupling constant  $\alpha \equiv \Delta(0)/k_B T_c$ , where  $\Delta(0)$  is the gap size at 0 K. It turns out that the  $C_{el}/\gamma T$  jumps for both  $x = 0$  and  $3$  can be well reproduced with  $\alpha = 1.88$ . This  $\alpha$  value is indeed larger than  $\alpha_{BCS} = 1.764$  of BCS theory [38], consistent with the trend in  $\lambda_{ep}$ . Overall, these results suggest that the  $\text{Cr}_{5+x}\text{Mo}_{35-x}\text{W}_{12}\text{Re}_{35}\text{Ru}_{13}\text{C}_{20}$  HEAs are weakly coupled, fully gapped superconductors.

Given that Cr is a magnetic element, it is natural to investigate the normal-state magnetic behavior of the  $\text{Cr}_{5+x}\text{Mo}_{35-x}\text{W}_{12}\text{Re}_{35}\text{Ru}_{13}\text{C}_{20}$  HEAs. Fig. 3(a) shows the  $\chi(T)$  curve measured under 5 T for the HEA with  $x = 6$ . With decreasing temperature from 300 K,  $\chi(T)$  decreases gradually but exhibits a upturn below 70 K. Notably, the whole curve is well fitted by the equation [40]

$$\chi = \chi_0 + AT^2 + \frac{C}{T - \Theta}, \quad (4)$$

where  $\chi_0$  is the temperature independent term,  $AT^2$  is the temperature dependent Pauli paramagnetism (due to the thermal depopulation of electronic states at the Fermi level),  $C$  is the Curie constant, and  $\Theta$  is the Weiss

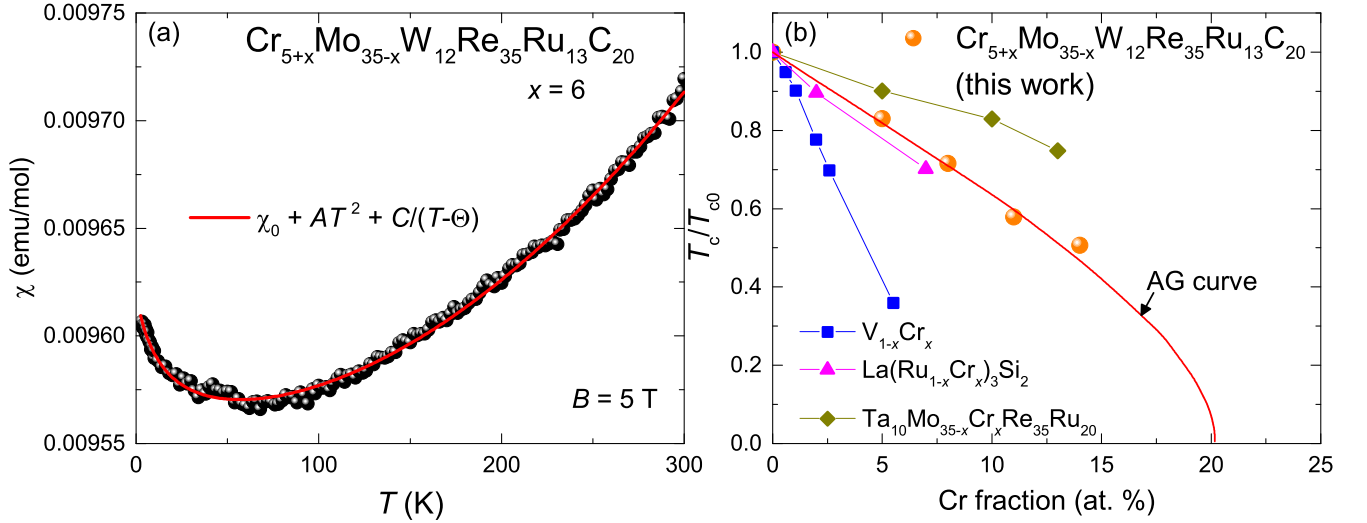


FIG. 3: (a) Temperature dependence of normal-state magnetic susceptibility for the  $\text{Cr}_{5+x}\text{Mo}_{35-x}\text{W}_{12}\text{Re}_{35}\text{Ru}_{13}\text{C}_{20}$  HEA with  $x = 6$ . The solid line is a fit to the data (see text for details). (b) Dependence of normalized  $T_c$  on the Cr atomic fraction for the  $\text{Cr}_{5+x}\text{Mo}_{35-x}\text{W}_{12}\text{Re}_{35}\text{Ru}_{13}\text{C}_{20}$  HEAs. The solid line denotes the curve predicted by the AG pair-breaking theory. The data for typical elemental and intermetallic superconductors are also included for comparison.

TABLE I: Parameters of the  $\text{Cr}_{5+x}\text{Mo}_{35-x}\text{W}_{12}\text{Re}_{35}\text{Ru}_{13}\text{C}_{20}$  HEAs.

Parameter	$x = 0$	$x = 3$	$x = 6$	$x = 9$
$a$ (Å)	6.7940(3)	6.7828(2)	6.7745(1)	6.7516(3)
Configurational entropy	$1.40R$	$1.45R$	$1.49R$	$1.51R$
Cr (at.%)	4.7(1)	8.1(1)	11.1(1)	13.3(1)
Mo (at.%)	33.5(1)	31.3(1)	28.5(1)	25.4(1)
W (at.%)	12.1(1)	11.4(1)	11.8(1)	11.0(1)
Re (at.%)	35.8(1)	34.9(1)	34.7(1)	35.7(1)
Ru (at.%)	13.9(1)	14.3(1)	13.9(1)	14.6(1)
$T_c$ (K)	5.49	4.73	3.83	3.35
$\gamma$ (mJ molatom $^{-1}$ K $^{-2}$ )	3.31	3.44	3.60	3.72
$\delta$ (mJ molatom $^{-1}$ K $^{-4}$ )	0.048	0.041	0.039	0.039
$\Theta_D$ (K)	343	362	368	368
$\lambda_{ep}$	0.63	0.60	0.56	0.55
$B_{c2}(0)$ (T)	9.7	8.4	7.3	5.3
$B_{c2}(0)/B_P(0)$	0.95	0.96	1.03	0.85
$\xi_{GL}(0)$ (nm)	5.8	6.3	6.7	7.9

temperature. The obtained  $\chi_0 = 9.55 \times 10^{-3}$  emu mol $^{-1}$ ,  $A = 1.78 \times 10^{-9}$  emu mol $^{-1}$  K $^{-2}$ ,  $C = 1.06 \times 10^{-3}$  emu K mol $^{-1}$ , and  $\Theta = -15.5$  K. Assuming that the  $C$  term is solely due to the Cr atoms, it gives an effective moment of  $0.28 \mu_B$  per Cr atom. The  $\chi(T)$  behavior is very similar for other  $x$  values, and applying the same analysis gives Cr effective moments varying between  $0.25$  and  $0.54 \mu_B$  (see Supplementary Fig. S2). These values are more than half or comparable to that in Cr metal [41].

The presence of local moments can induce spin-flip scattering, which breaks the Cooper pairs and leads

to reduction in  $T_c$ . This is indeed the case for the  $\text{Cr}_{5+x}\text{Mo}_{35-x}\text{W}_{12}\text{Re}_{35}\text{Ru}_{13}\text{C}_{20}$  HEAs, as illustrated in the plot of normalized  $T_c/T_{c0}$  against Cr fraction in Fig. 3(b). One can see that the negative slope of  $T_c/T_{c0}$  is close to that in  $\text{La}(\text{Ru}_{1-x}\text{Cr}_x)_3\text{Si}_2$  [42], and lies between  $\text{V}_{1-x}\text{Cr}_x$  [43] and tetragonal  $\text{Ta}_{10}\text{Mo}_{35-x}\text{Cr}_x\text{Re}_{35}\text{Ru}_{20}$  HEAs [30]. According to the Abrikosov-Gorkov (AG) theory [44] for magnetic pair breaking, the depression rate of  $T_c/T_{c0}$  can be described by the universal relation

$$\ln(T_c/T_{c0}) = \Psi\left(\frac{1}{2}\right) - \Psi\left(\frac{1}{2} + \alpha\right), \quad (5)$$

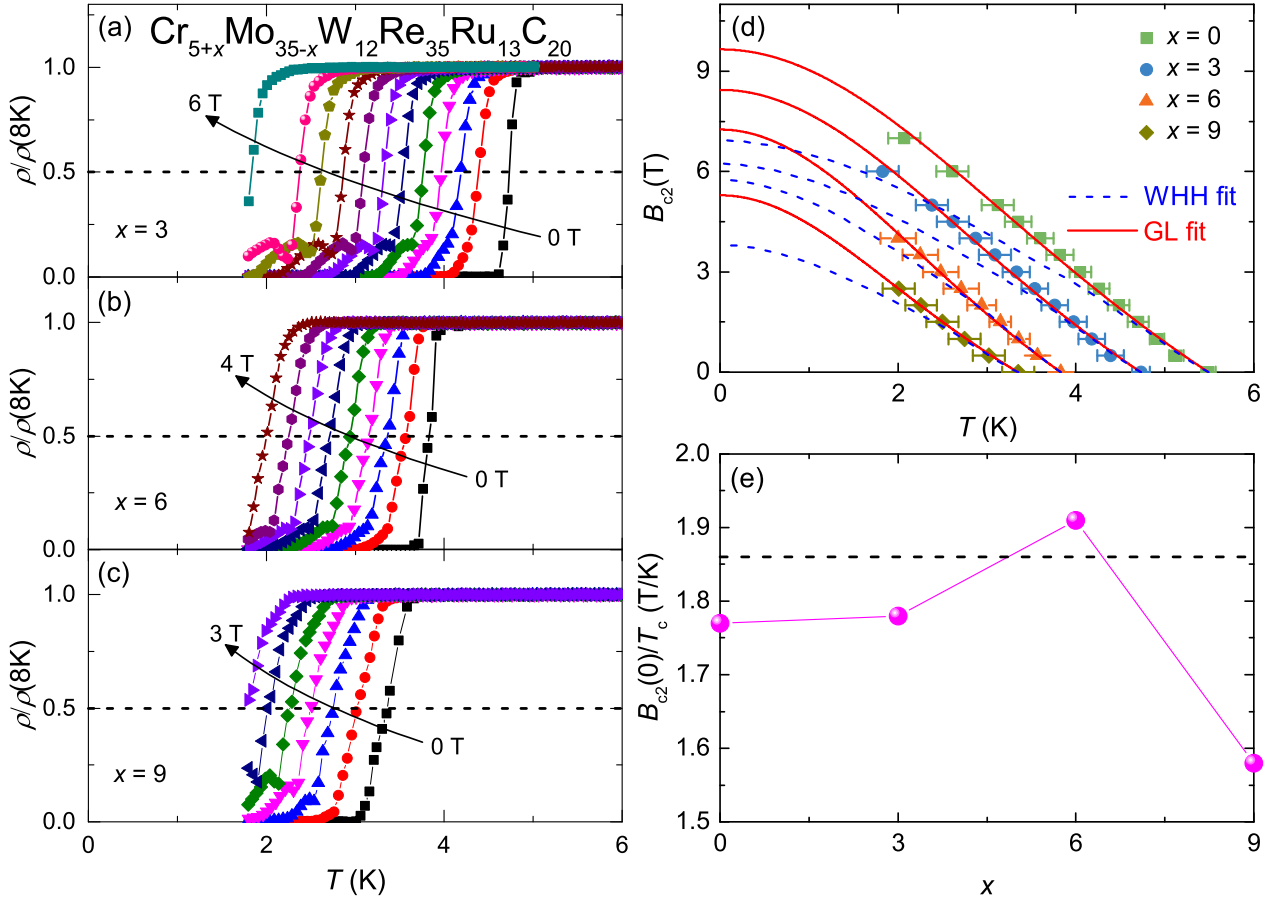


FIG. 4: (a-c) Resistive transition under various magnetic fields for the  $\text{Cr}_{5+x}\text{Mo}_{35-x}\text{W}_{12}\text{Re}_{35}\text{Ru}_{13}\text{C}_{20}$  HEAs with  $x = 3, 6$ , and  $9$ , respectively. In each panel, the arrow marks the field increasing direction. (d) Upper critical field versus temperature phase diagrams for the HEAs. The dashed and solid lines are fits by the WHH and GL models, respectively. (e)  $x$  dependence of the  $B_{c2}(0)/T_c$  ratio for the HEAs. The horizontal dashed line denotes the Pauli paramagnetic limit of  $B_P(0)/T_c = 1.86$  T/K.

where  $\Psi$  is the digamma function and  $\alpha$  is the pair breaking parameter. The  $T_c/T_{c0}$  data for the  $\text{Cr}_{5+x}\text{Mo}_{35-x}\text{W}_{12}\text{Re}_{35}\text{Ru}_{13}\text{C}_{20}$  HEAs obeys well the AG formalism and the critical Cr fraction, at which  $T_c/T_{c0}$  becomes zero, is estimated to be about 20.2%. Note that this value is only half that for the  $\text{Ta}_{10}\text{Mo}_{35-x}\text{Cr}_x\text{Re}_{35}\text{Ru}_{20}$  HEAs [30], implying a stronger pair breaking effect in the former compared with that in the latter.

We now turn the attention to the upper critical field  $B_{c2}$  of the  $\text{Cr}_{5+x}\text{Mo}_{35-x}\text{W}_{12}\text{Re}_{35}\text{Ru}_{13}\text{C}_{20}$  HEAs. Fig. 4(a)-(c) show the temperature dependencies of resistivity under various magnetic fields for  $x = 3, 6$ , and  $9$ , respectively. For all cases, the resistive transition is suppressed toward lower temperatures as the field increases. Nevertheless, a resistivity tail is observed in the intermediate to high-field region, which is reminiscent of that seen in the  $\text{Ta}_{10}\text{Mo}_5\text{W}_{30}\text{Re}_{35}\text{Ru}_{20}\text{C}_{20}$  HEA [34]. In fact, such anomaly is typical for  $\beta$ -Mn type superconductors containing carbon [45, 46], which often precipitates at the grain boundaries and results in weak links between the superconducting grains. As such, the  $T_c$  under field

is determined by the same criterion as that at zero field and the resulting  $B_{c2}$  versus  $T$  phase diagrams are summarized in Fig. 4(d). The  $B_{c2}(T)$  data shows upward deviation from the Werthamer-Hohenberg-Helfand theory [47], especially at low temperature, but can be well fitted by the Ginzburg-Landau (GL) model

$$B_{c2}(T) = B_{c2}(0) \frac{1 - t^2}{1 + t^2}, \quad (6)$$

where  $t = T/T_c$  is the reduced temperature. Extrapolating the data to 0 K yields the zero-temperature upper critical field  $B_{c2}(0) = 9.7$  T, 8.4 T, 7.3 T, and 5.3 T for  $x = 0, 3, 6$ , and  $9$ , respectively. With  $B_{c2}(0)$ , the Ginzburg-Landau (GL) coherence length  $\xi_{GL}(0)$  is found to vary from 5.8 nm to 7.9 nm based on the equation

$$\xi_{GL}(0) = \sqrt{\frac{\Phi_0}{2\pi B_{c2}(0)}}, \quad (7)$$

where  $\Phi_0 = 2.07 \times 10^{-15}$  Wb is the flux quantum.

In Fig. 4(e), we plot the ratio of  $B_{c2}(0)/T_c$  as a function of  $x$  for the  $\text{Cr}_{5+x}\text{Mo}_{35-x}\text{W}_{12}\text{Re}_{35}\text{Ru}_{13}\text{C}_{20}$



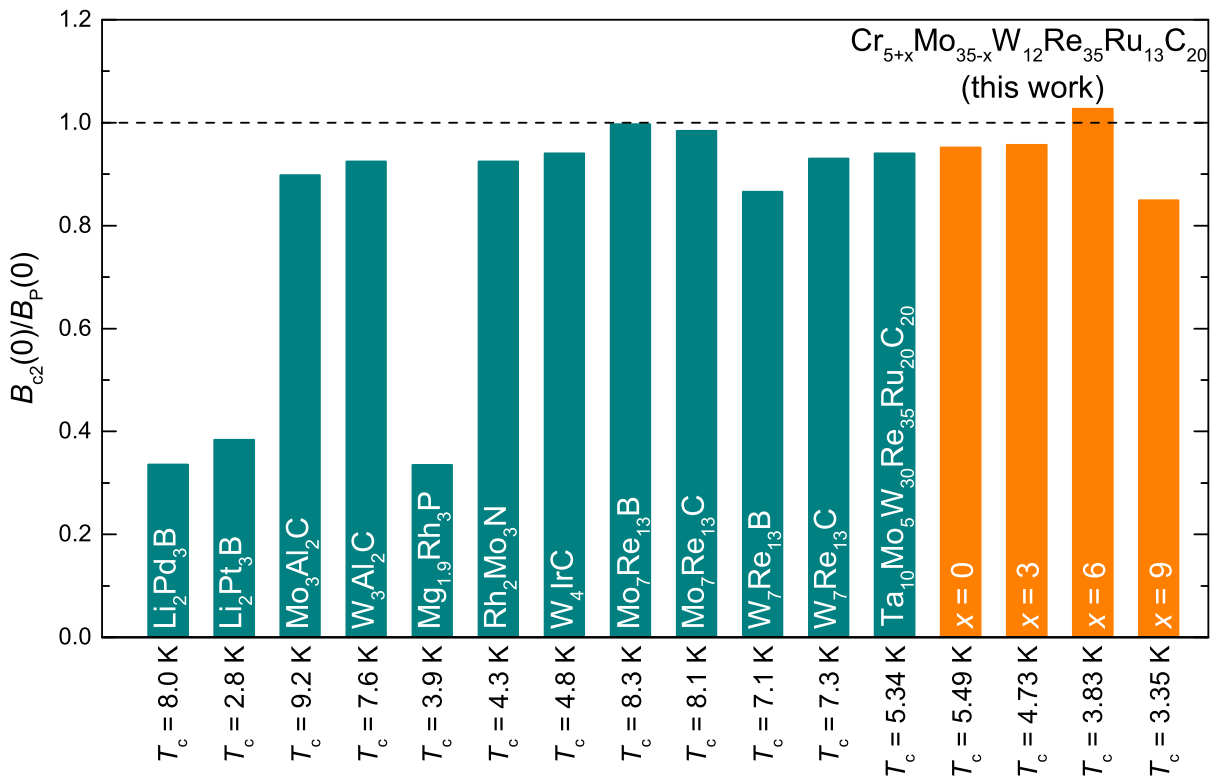


FIG. 5:  $B_{c2}(0)/B_P(0)$  ratios for various  $\beta$ -Mn type superconductors including the  $\text{Cr}_{5+x}\text{Mo}_{35-x}\text{W}_{12}\text{Re}_{35}\text{Ru}_{13}\text{C}_{20}$  HEAs. The horizontal line represents the level of  $B_{c2}(0)/B_P(0) = 1$ .

HEAs. Remarkably,  $B_{c2}(0)/T_c$  attains large values above 1.58 T/K and exhibits a maximum of 1.91 T/K at  $x = 6$ . In fact, this maximum not only is slightly larger than the Pauli paramagnetic limit of  $B_P(0)/T_c = 1.86$  T/K [48], but also is the highest among  $\beta$ -Mn type superconductors. This can be seen more clearly in Fig. 5, which presents a comparison of  $B_{c2}(0)/B_P(0)$  ratios between various superconductors of this family [34, 45, 46, 49–55]. Indeed, compared with nonmagnetic  $\beta$ -Mn type carbide superconductors, the  $\text{Cr}_{5+x}\text{Mo}_{35-x}\text{W}_{12}\text{Re}_{35}\text{Ru}_{13}\text{C}_{20}$  HEA with  $x = 6$  has a considerably smaller  $T_c$  yet a obviously larger  $B_{c2}(0)/B_P(0)$  ratio of  $\sim 1.03$ . Also, the  $B_{c2}(0)/B_P(0)$  ratios of the HEAs with  $x = 0$  (0.95) and 3 (0.96) are slightly larger than those of  $\text{Ta}_{10}\text{Mo}_5\text{W}_{30}\text{Re}_{35}\text{Ru}_{20}\text{C}_{20}$  (0.94) and  $\text{W}_4\text{IrC}$  (0.94) with similar  $T_c$  values. At the highest  $x$  of 9, however, the  $B_{c2}(0)/B_P(0)$  ratio of the  $\text{Cr}_{5+x}\text{Mo}_{35-x}\text{W}_{12}\text{Re}_{35}\text{Ru}_{13}\text{C}_{20}$  HEA decreases to 0.85, which turns out to be the smallest among  $\beta$ -Mn type carbide superconductors.

For noncentrosymmetric superconductors, the ratio of  $B_{c2}(0)/B_P(0)$  might be an indication of the contribution from the spin-triplet pairing. In this regard, it seems that the spin-triplet pairing component is enhanced within a certain range of Cr content. However, this is unlikely since the spin-triplet pairing is unfavored in strongly disordered systems such as HEAs. Instead, it is prudent to note that  $B_{c2}(0)/T_c$  is proportional to

$\gamma\rho_N$  in the dirty limit [56], where  $\rho_N$  is the normal-state resistivity value just above  $T_c$ . Hence it is reasonable to speculate that the increases in both  $\rho_N$  and  $\gamma$  are responsible for the enhancement of  $B_{c2}(0)/T_c$  in  $\text{Cr}_{5+x}\text{Mo}_{35-x}\text{W}_{12}\text{Re}_{35}\text{Ru}_{13}\text{C}_{20}$  HEAs with  $x \leq 6$ . This is reminiscent of the cases in  $(\text{V}_{0.5}\text{Nb}_{0.5})_{3-x}\text{Mo}_x\text{Al}_{0.5}\text{Ga}_{0.5}$  HEAs [27] and several superconducting amorphous transition metal alloys [57]. The decrease of  $B_{c2}(0)/T_c$  at a higher  $x = 9$  may be related to magnetic interaction of Cr, and the clarification of its origin is definitively of future interest, in particular given that the interplay between magnetism and superconductivity in disordered noncentrosymmetric systems remains poorly understood.

In summary, we have synthesized and characterized a series of new Cr-bearing  $\text{Cr}_{5+x}\text{Mo}_{35-x}\text{W}_{12}\text{Re}_{35}\text{Ru}_{13}\text{C}_{20}$  HEAs with  $0 \leq x \leq 9$ . In the whole range of  $x$ , the HEAs are found to crystallize in the noncentrosymmetric cubic  $\beta$ -Mn type structure and exhibit bulk superconductivity. With increasing  $x$ , the lattice constant shrinks and  $T_c$  is suppressed from 5.49 K to 3.35 K due to the magnetic pair breaking caused by Cr moments. For all these HEAs, the  $B_{c2}(0)$  is comparable to the  $B_P(0)$  and the ratio of  $B_{c2}(0)/B_P(0)$  achieves a maximum of  $\sim 1.03$  for  $x = 6$ , which is among the highest for  $\beta$ -Mn type superconductors. Our results call for further exploration of noncentrosymmetric HEA superconductors containing magnetic elements, which may help to better understand the interplay between magnetism, lack of inversion

symmetry and superconductivity in strongly disordered alloy systems.

Sciences for technical assistance in SEM measurements. The work at Zhejiang University is supported by the National Natural Science Foundation of China (12050003).

## ACKNOWLEDGEMENT

We acknowledge financial support by the foundation of Westlake University and the Service Center for Physical

- 
- [1] J.-W. Yeh, S.-K. Chen, S.-J. Lin, J.-Y. Gan, T.-S. Chin, T.-T. Shun, C.-H. Tsau, S.-Y. Chang, Nanostructured high-entropy alloys with multiple principal elements: novel alloy design concepts and outcomes, *Adv. Eng. Mater.* 6 (2004) 299–303.
- [2] Y. Ye, Q. Wang, J. Lu, C. Liu, Y. Yang, High-entropy alloy: challenges and prospects, *Mater. Today* 19 (2016) 349–362.
- [3] D. B. Miracle, O. N. Senkov, A critical review of high entropy alloys and related concepts, *Acta Mater.* 122 (2017) 448–511.
- [4] W. Zhang, P. K. Liaw, Y. Zhang, Science and technology in high-entropy alloys, *Sci. China Mater.* 61 (2018) 2–22.
- [5] E. P. George, D. Raabe, R. O. Ritchie, High-entropy alloys, *Nat. Rev. Mater.* 4 (2019) 515–534.
- [6] W. Li, D. Xie, D. Li, Y. Zhang, Y. Gao, P. K. Liaw, Mechanical behavior of high-entropy alloys, *Prog. Mater. Sci.* 118 (2021) 100777.
- [7] X. Wang, W. Guo, Y. Fu, High-entropy alloys: emerging materials for advanced functional applications, *J. Mater. Chem. A* 9 (2021) 663–701.
- [8] C. Lee, Y. Chou, G. Kim, M. C. Gao, K. An, J. Brechtel, C. Zhang, W. Chen, J. D. Poplawsky, G. Song, Y. Ren, Y.-C. Chou, P. K. Liaw, Lattice-distortion-enhanced yield strength in a refractory high-entropy alloy, *Adv. Mater.* 32 (2020) 2004029.
- [9] Z. An, S. Mao, Y. Liu, L. Wang, H. Zhou, B. Gan, Z. Zhang, X. Han, A novel hfnbtativ high-entropy alloy of superior mechanical properties designed on the principle of maximum lattice distortion, *J. Mater. Sci. Technol.* 79 (2021) 109–117.
- [10] Z. Tang, L. Huang, W. He, P. K. Liaw, Alloying and processing effects on the aqueous corrosion behavior of high-entropy alloys, *Entropy* 16 (2014) 895–911.
- [11] Y. Zhang, T. T. Zuo, Z. Tang, M. C. Gao, K. A. Dahmen, P. K. Liaw, Z. P. Lu, Microstructures and properties of high-entropy alloys, *Prog. Mater. Sci.* 61 (2014) 1–93.
- [12] Y. Shi, B. Yang, X. Xie, J. Brechtel, K. A. Dahmen, P. K. Liaw, Corrosion of  $Al_xCoCrFeNi$  high-entropy alloys: Al-content and potential scan-rate dependent pitting behavior, *Corros. Sci.* 119 (2017) 33–45.
- [13] N. Hua, W. Wang, Q. Wang, Y. Ye, S. Lin, L. Zhang, Q. Guo, J. Brechtel, P. K. Liaw, Mechanical, corrosion, and wear properties of biomedical Ti–Zr–Nb–Ta–Mo high entropy alloys, *J. Alloy. Compd.* 861 (2021) 157997.
- [14] M. Vaidya, K. Guruvidyathri, B. Murty, Phase formation and thermal stability of  $CoCrFeNi$  and  $CoCrFeMnNi$  equiatomic high entropy alloys, *J. Alloy. Compd.* 774 (2019) 856–864.
- [15] T. E. Whitfield, E. J. Pickering, L. R. Owen, O. N. Senkov, D. B. Miracle, H. J. Stone, N. G. Jones, An assessment of the thermal stability of refractory high entropy superalloys, *J. Alloy. Compd.* 857 (2021) 157583.
- [16] Y. Yuan, Y. Wu, X. Tong, H. Zhang, H. Wang, X. Liu, L. Ma, H. Suo, Z. Lu, Rare-earth high-entropy alloys with giant magnetocaloric effect, *Acta Mater.* 125 (2017) 481–489.
- [17] J. Y. Law, Á. Díaz-García, L. M. Moreno-Ramírez, V. Franco, Increased magnetocaloric response of  $FeMnNiGeSi$  high-entropy alloys, *Acta Mater.* 212 (2021) 116931.
- [18] F. Von Rohr, M. J. Winiarski, J. Tao, T. Klimczuk, R. J. Cava, Effect of electron count and chemical complexity in the Ta-Nb-Hf-Zr-Ti high-entropy alloy superconductor, *Proc. Natl. Acad. Sci. U. S. A.* 113 (2016) E7144–E7150.
- [19] J. Guo, H. Wang, F. Von Rohr, Z. Wang, S. Cai, Y. Zhou, K. Yang, A. Li, S. Jiang, Q. Wu, R. J. Cava, L. Sun, Robust zero resistance in a superconducting high-entropy alloy at pressures up to 190 gpa, *Proc. Natl. Acad. Sci. U. S. A.* 114 (2017) 13144–13147.
- [20] L. Sun, R. J. Cava, High-entropy alloy superconductors: Status, opportunities, and challenges, *Phys. Rev. Mater.* 3 (2019) 090301.
- [21] P. Koželj, S. Vrtnik, A. Jelen, S. Jazbec, Z. Jagličić, S. Maiti, M. Feuerbacher, W. Steurer, J. Dolinšek, Discovery of a superconducting high-entropy alloy, *Phys. Rev. Lett.* 113 (2014) 107001.
- [22] S. Marik, M. Varghese, K. Sajilesh, D. Singh, R. Singh, Superconductivity in equimolar Nb-Re-Hf-Zr-Ti high entropy alloy, *J. Alloy. Compd.* 769 (2018) 1059–1063.
- [23] K. Stolze, J. Tao, F. O. Von Rohr, T. Kong, R. J. Cava, Sc–Zr–Nb–Rh–Pd and Sc–Zr–Nb–Ta–Rh–Pd high-entropy alloy superconductors on a CsCl-type lattice, *Chem. Mater.* 30 (2018) 906–914.
- [24] S. Marik, K. Motla, M. Varghese, K. Sajilesh, D. Singh, Y. Breard, P. Boullay, R. Singh, Superconductivity in a new hexagonal high-entropy alloy, *Phys. Rev. Mater.* 3 (2019) 060602.
- [25] Y.-S. Lee, R. J. Cava, Superconductivity in high and medium entropy alloys based on  $MoReRu$ , *Physica C* 566 (2019) 1353520.
- [26] B. Liu, J. Wu, Y. Cui, Q. Zhu, G. Xiao, S. Wu, G. Cao, Z. Ren, Superconductivity in hexagonal Nb-Mo-Ru-Rh-Pd high-entropy alloys, *Scripta Mater.* 182 (2020) 109–113.
- [27] J. Wu, B. Liu, Y. Cui, Q. Zhu, G. Xiao, H. Wang, S. Wu, G. Cao, Z. Ren, Polymorphism and superconductivity in the V-Nb-Mo-Al-Ga high-entropy alloys, *Sci. China Mater.* 63 (2020) 823–831.

- [28] A. Yamashita, T. D. Matsuda, Y. Mizuguchi, Synthesis of new high-entropy alloy-type  $\text{Nb}_3(\text{Al}, \text{Sn}, \text{Ge}, \text{Ga}, \text{Si})$  superconductors, *J. Alloy. Compd.* 868 (2021) 159233.
- [29] B. Liu, J. Wu, Y. Cui, Q. Zhu, G. Xiao, H. Wang, S. Wu, G. Cao, Z. Ren, Formation and superconductivity of single-phase high-entropy alloys with a tetragonal structure, *ACS Appl. Electron. Mater.* 2 (2020) 1130–1137.
- [30] B. Liu, J. Wu, Y. Cui, Q. Zhu, G. Xiao, S. Wu, G.-h. Cao, Z. Ren, Superconductivity and paramagnetism in Cr-containing tetragonal high-entropy alloys, *J. Alloy. Compd.* 869 (2021) 159293.
- [31] Q. Zhu, G. Xiao, Y. Cui, W. Yang, S. Song, G.-H. Cao, Z. Ren, Structural transformation and superconductivity in carbon-added hexagonal high-entropy alloys, *J. Alloy. Compd.* 909 (2022) 164700.
- [32] K. Stolze, F. A. Cevallos, T. Kong, R. J. Cava, High-entropy alloy superconductors on an  $\alpha$ -Mn lattice, *J. Mater. Chem. C* 6 (2018) 10441–10449.
- [33] B. Liu, J. Wu, Y. Cui, Q. Zhu, G. Xiao, S. Wu, G.-h. Cao, Z. Ren, Structural evolution and superconductivity tuned by valence electron concentration in the Nb-Mo-Re-Ru-Rh high-entropy alloys, *J. Mater. Sci. Technol.* 85 (2021) 11–17.
- [34] G. Xiao, Q. Zhu, W. Yang, Y. Cui, S. Song, G.-H. Cao, Z. Ren, Centrosymmetric to noncentrosymmetric structural transformation in a superconducting high-entropy alloy due to carbon addition, *Sci. China Mater.* (2022). URL: <https://doi.org/10.1007/s40843-022-2144-x>.
- [35] V. Petříček, M. Dušek, L. Palatinus, Crystallographic computing system JANA2006: general features, *Z. Kristallogr.* 229 (2014) 345–352.
- [36] L. Pauling, Atomic radii and interatomic distances in metals, *J. Am. Chem. Soc.* 69 (1947) 542–553.
- [37] W. L. McMillan, Transition temperature of strongly-coupled superconductors, *Phys. Rev.* 167 (1968) 331–344.
- [38] J. Bardeen, L. N. Cooper, J. R. Schrieffer, Theory of superconductivity, *Phys. Rev.* 108 (1957) 1175–1204.
- [39] D. C. Johnston, Elaboration of the  $\alpha$ -model derived from the BCS theory of superconductivity, *Supercond. Sci. Technol.* 26 (2013) 115011.
- [40] H. Sakurai, K. Takada, S. Yoshii, T. Sasaki, K. Kindo, E. Takayama-Muromachi, Unconventional upper- and lower-critical fields and normal-state magnetic susceptibility of the superconducting compound  $\text{Na}_{0.35}\text{CoO}_2 \cdot 1.3\text{H}_2\text{O}$ , *Phys. Rev. B* 68 (2003) 132507.
- [41] A. Arrott, S. Werner, H. Kendrick, Neutron-diffraction study of dilute chromium alloys with iron, *Phys. Rev.* 153 (1967) 624–631.
- [42] B. Li, S. Li, H.-H. Wen, Chemical doping effect in the  $\text{LaRu}_3\text{Si}_2$  superconductor with a kagome lattice, *Phys. Rev. B* 94 (2016) 094523.
- [43] J. Muller, Superconductivity in mixed crystals of vanadium with transition elements, *Helv. Phys. Acta* 32 (1959) 141.
- [44] A. A. Abrikosov, L. P. Gor'kov, Contribution to the theory of superconducting alloys with paramagnetic impurities, *Sov. Phys. JETP* 12 (1961) 1243–1253.
- [45] K. Kawashima, A. Kawano, T. Muranaka, J. Akimitsu, Superconductivity in intermetallic  $\text{W}_7\text{Re}_{13}\text{X}$  ( $\text{X} = \text{B}$  and  $\text{C}$ ) compounds, *J. Phys. Soc. Jpn.* 74 (2005) 700–704.
- [46] Q. Zhu, G. Xiao, Y. Cui, W. Yang, S. Wu, G.-h. Cao, Z. Ren,  $\text{W}_4\text{IrC}_{1-x}$ : a new noncentrosymmetric superconductor with a cubic  $\beta$ -Mn type structure, *J. Mater. Chem. C* 10 (2022) 6070–6077.
- [47] N. Werthamer, E. Helfand, P. Hohenberg, Temperature and purity dependence of the superconducting critical field,  $H_{c2}$ . III. Electron spin and spin-orbit effects, *Phys. Rev.* 147 (1966) 295–302.
- [48] A. M. Clogston, Upper limit for the critical field in hard superconductors, *Phys. Rev. Lett.* 9 (1962) 266–267.
- [49] K. Togano, P. Badica, Y. Nakamori, S. Orimo, H. Takeya, K. Hirata, Superconductivity in the metal rich Li-Pd-B ternary boride, *Phys. Rev. Lett.* 93 (2004) 247004.
- [50] P. Badica, T. Kondo, K. Togano, Superconductivity in a new pseudo-binary  $\text{Li}_2\text{B}(\text{Pd}_{1-x}\text{Pt}_x)_3$  ( $x = 0-1$ ) boride system, *J. Phys. Soc. Jpn.* 74 (2005) 1014–1019.
- [51] A. Karki, Y. Xiong, I. Vekhter, D. Browne, P. Adams, D. Young, K. Thomas, J. Y. Chan, H. Kim, R. Prozorov, Structure and physical properties of the noncentrosymmetric superconductor  $\text{Mo}_3\text{Al}_2\text{C}$ , *Phys. Rev. B* 82 (2010) 064512.
- [52] T. Ying, Y. Qi, H. Hosono, Superconductivity with strong electron-phonon coupling in noncentrosymmetric  $\text{W}_3\text{Al}_2\text{C}$ , *Phys. Rev. B* 100 (2019) 094522.
- [53] A. Iyo, I. Hase, H. Fujihisa, Y. Gotoh, N. Takeshita, S. Ishida, H. Ninomiya, Y. Yoshida, H. Eisaki, K. Kawashima, Superconductivity induced by mg deficiency in noncentrosymmetric phosphide  $\text{Mg}_2\text{Rh}_3\text{P}$ , *Phys. Rev. Mater.* 3 (2019) 124802.
- [54] W. Wei, G. J. Zhao, D. R. Kim, C. Jin, J. L. Zhang, L. Ling, L. Zhang, H. Du, T. Y. Chen, J. Zang, M. Tian, C. L. Chien, Y. Zhang,  $\text{Rh}_2\text{Mo}_3\text{N}$ : Noncentrosymmetric s-wave superconductor, *Phys. Rev. B* 94 (2016) 104503.
- [55] K. Kawashima, T. Muranaka, J. Akimitsu, Superconductivity in intermetallic compound  $\text{Mo}_7\text{Re}_{13}\text{X}$  ( $\text{X} = \text{B}, \text{C}$ ), *Sci. Technol. Adv. Mater.* 7 (2006) 9–11.
- [56] T. P. Orlando, E. J. McNiff, S. Foner, M. R. Beasley, Critical fields, pauli paramagnetic limiting, and material parameters of  $\text{Nb}_3\text{Sn}$  and  $\text{V}_3\text{Si}$ , *Phys. Rev. B* 19 (1979) 4545–4561.
- [57] M. Tenhover, W. Johnson, C. Tsuei, Upper critical fields of amorphous transition metal based alloys, *Solid State Commun.* 38 (1981) 53–57.